AIAA JOURNAL
Vol. 45, No. 9, September 2007

Diode-Laser Sensor for Air-Mass Flux 2: Nonuniform Flow Modeling and Aeroengine Tests

Kent H. Lyle,* Jay B. Jeffries,† and Ronald K. Hanson‡
Stanford University, Stanford, California 94305
and
Michael Winter§
Pratt and Whitney Aircraft, United Technologies Corporation, East Hartford, Connecticut 06108

DOI: 10.2514/1.27683

Diode-laser mass flux sensor measurements are performed with a readout rate of 1 Hz in a Pratt and Whitney turbofan aeroengine during ground testing. The installation of the fiber-coupled sensor into the engine is described. The sensor's line-of-sight path has significant deviations from a uniform flow, and potential errors from these nonuniformities in the magnitude and direction of the velocity are investigated. The velocity is inferred from the Doppler shift of the wavelength-scanned line shape of molecular oxygen absorption near 764 nm using wavelength-modulation spectroscopy with detection at twice the modulation frequency ($2f$). The distortion of the wavelength-modulation spectroscopy-$2f$ line shape from variations in the magnitude of the velocity is found to be small at subsonic velocities, which leads to accurate determination of the line center of the Doppler-shifted line shape. The apparent velocity is then corrected to account for nonuniformities using potential flow approximations. With this correction, the diode-laser sensor agrees (∼1%) with concurrent measurements of the calibrated mass flow to the aeroengine.

Nomenclature

a	=	amplitude of laser WMS modulation, cm^{-1}
c	=	speed of light in a vacuum, m/s
f	=	laser modulation frequency, Hz
L	=	laser path length through absorbing medium, cm
m	=	modulation depth, $m \equiv a/\Gamma$
$\dot{m}_{\text{meas}}$	=	time-averaged measured mass flow, kg/s
U_0	=	freestream gas velocity, m/s
$U_{\parallel}$	=	component of local velocity parallel to laser beam, m/s
Γ	=	half-width at half-maximum of direct absorption line shape, cm^{-1}
$\Delta\nu$	=	Doppler-shifted difference between line-center frequencies, cm^{-1}
$\varepsilon_{\%,\text{ave}}$	=	percent accuracy of time-averaged mass flux measurement
$\varepsilon_{\%,1\text{ s}}$	=	estimated percent accuracy for 1-s mass flux measurements
θ	=	crossing half-angle between two beams in measurement test section
ν	=	optical frequency, cm^{-1}
ν_0	=	line-center frequency in absence of Doppler shift, cm^{-1}
ρ	=	gas density, kg/m^3
$\sigma_{\%}$	=	percent 1-s standard deviation of mass flux measurement

Received 6 September 2006; revision received 22 January 2007; accepted for publication 27 February 2007.

*Graduate Research Assistant, Mechanical Engineering; Present Address: GE Aircraft Engines, Cincinnati, OH. Member AIAA.
†Senior Research Engineer, Mechanical Engineering. Associate Fellow AIAA.
‡Professor, Mechanical Engineering. Fellow AIAA.
§Program Manager, Pratt and Whitney. Member AIAA.

I. Introduction

THE preceding paper [1] describes the design and laboratory testing of a tunable diode-laser-based sensor for air-mass flux, that is, the product of velocity and density. This sensor relies on optical absorption of a fiber-coupled laser near 764 nm that probes the PP(11,11) oxygen transition. The introductory material, references to previous work, description of fundamentals underlying the sensor design, the assembly of a prototype sensor, and test measurements of air-mass flux in a wind tunnel are all described in the previous paper [1] and will not be repeated here. The wind-tunnel results [1] were obtained in a laboratory environment with a highly uniform flowfield; however, the flowfield will not be uniform in practical applications such as the turbofan inlet used for the demonstration measurements reported here. Thus precise interpretation of the measured values for velocity and density from a line-of-sight diode-laser absorption sensor must take these nonuniformities into account. The velocity is inferred from the Doppler shift of the wavelength-scanned line shape of a single, isolated oxygen absorption transition using wavelength-modulation spectroscopy (WMS) with detection at twice the modulation frequency ($2f$). In this paper, the potential distortion of the wavelength-scanned WMS-$2f$ line shape from such nonuniformities is investigated and found to be small at subsonic velocities. A correction to the apparent velocity is determined using a simple model based on potential flow approximations, which provides a methodology which could be extended to a wide variety of other applications.

The diode-laser mass flux sensor from [1] is demonstrated in the ground test of a PW6000 turbofan engine at Pratt and Whitney's ground-test facility at East Hartford, Connecticut, and the measurement results are compared with mass flux extracted from traditional test-stand instrumentation that uses total and static pressure and temperature probes [2–5]. The diode-laser sensor provided real-time 1 Hz mass flow measurements; in this context, "real time" refers to the fact that the absorption data are reduced to mass flow without postprocessing. The 1 Hz measurement rate of the diode-laser sensor is significantly faster than the multiminute measurement rates of the traditional ground-test instrumentation. With correction of the apparent velocity for flow nonuniformities, the measurements agreed well with concurrent measurements of the intake flow into the engine using the test-stand instrumentation.

Although the nonuniformity correction was postprocessed, future implementations of the sensor could include these corrections to provide real-time mass flux measurements. The diode-laser sensor measured the time-averaged mass flow to within 0.7% of the test-stand instrumentation at 100 m/s during a ground test of this commercial engine.

II. Flowfield Nonuniformities and Line Shape Distortion

The diode-laser sensor from [1] uses a combination of wavelength-scanned direct absorption and scanned WMS $2f$. The direct absorption scans are used for the density measurement, in which the integrated area calculated from a Voigt curve fit is directly proportional to the gas density, similar to the method employed by Miller et al. [6]. Scanned WMS $2f$ is used for the velocity measurement and affords much higher precision than would be possible with direct absorption. For the aeroengine measurements, the wavelength scan rate is 100 Hz and the modulation frequency is set at 20 kHz. Cumulative scan averaging is used to reduce the amount of noise present during each 1 Hz measurement cycle. A more detailed description of the sensor architecture can be found in [1].

The ideal environment for making Doppler velocity measurements has a measurement section with a constant cross-sectional area and does not include any solid bodies which deflect the flow. In the absence of boundary layers, the velocity field in such a facility can be completely uniform at all points in the measurement section, producing a constant Doppler frequency shift for an absorption line along the entire path. Figure 1 illustrates the velocity sensor concept with using two laser beams crossing at an angle 2θ, and the Doppler shift for a transition at frequency ν_0 is given for a uniform velocity by

$$\Delta\nu = \frac{(2\sin\theta)U}{c}\nu_0 \tag{1}$$

where $\Delta\nu$ (cm^{-1}) is the shift of the line-center frequency, ν_0 (cm^{-1}) is the unshifted line center, c is the speed of light (3×10^8 m/s), and U (m/s) is the uniform velocity. However, in real applications, there are often sources of flow nonuniformities as illustrated in Fig. 1 by the cone obstruction in the duct, the stagnant regions between the windows and the lasers/detectors, and the sidewall boundary layers. Other potential sources of nonuniformity of the flow velocity along the laser line of sight (LOS) are changes in the area of the flow duct.

For the case in which the nature of the flow nonuniformity is well understood, a model can be used to determine the numerically calculated mean velocity across the path, so that a simple correlation can be developed to correct each measurement to the desired mean axial freestream velocity. Most simply this approach assumes that the resulting absorption waveforms faithfully reflect the numerically averaged velocity across the measurement path without any distortion in absorption line shape. However, this may not be the case, as illustrated by Fig. 2a. This figure shows the individual absorbance from a measurement path of 1.5 m with 25% of the path in stagnant gas and 75% of the path having a plug flow velocity of 1000 m/s (i.e., 25% of the absorption has no Doppler shift and 75% of the absorption has a Doppler shift of 0.0436 cm^{-1}). The combined absorbance curve shown in Fig. 2b consequently exhibits slight

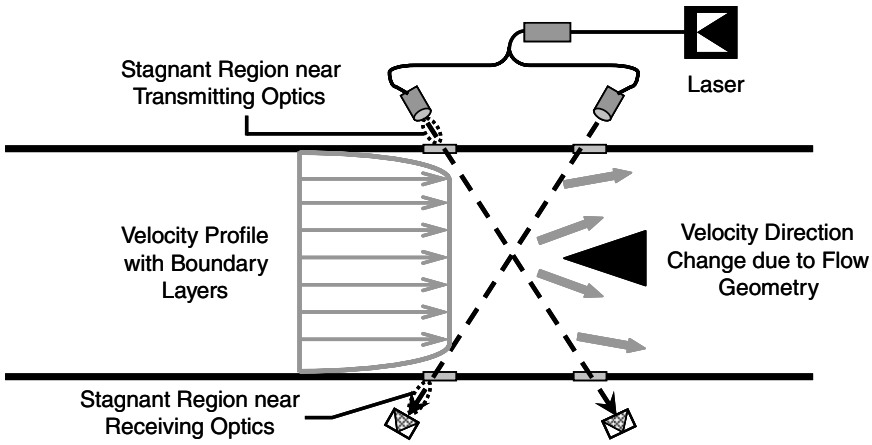

Fig. 1 Schematic of example velocity measurement with nonuniformities.

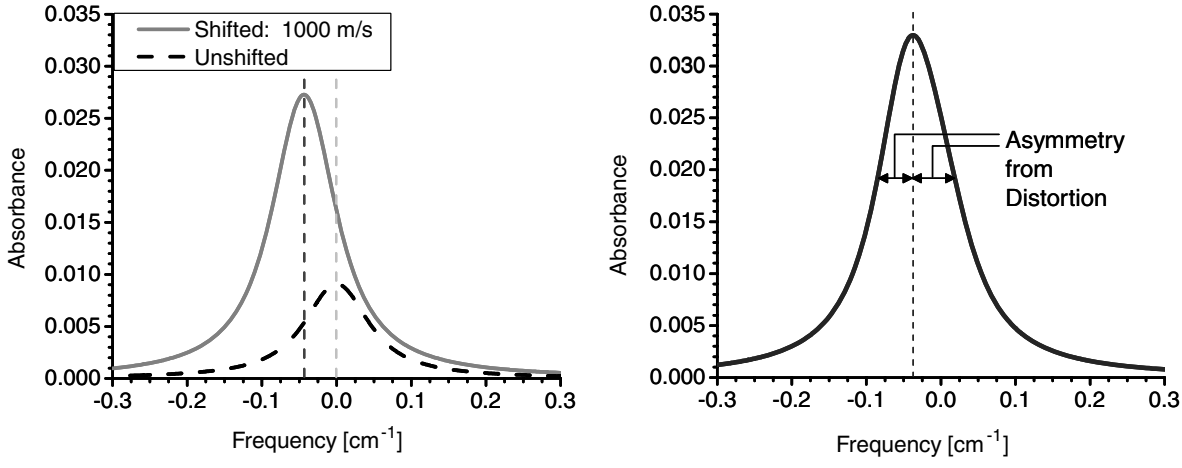

Fig. 2 Absorbance from 1.5 m path with 25% stagnant gas and 75% with a plug flow velocity of 1000 m/s. a) illustrates the absorption line shapes for the two segments of the path with their unequal Doppler shifts; b) combined absorbance of the total optical path.

asymmetric distortion, and it would be expected that the frequency shift inferred from two such distorted mirror-image line shapes would differ from the mean axial freestream velocity. We will thus investigate here the potential for such nonuniformities to skew the absorbance and contribute an error to the measured velocity.

Allen et al. [7] investigated the effect of flow nonuniformities on the measured Doppler shift for various simulated flowfields based on direct absorption, using a crossing angle of $2\theta = 90$ deg. They found no appreciable distortion of the feature line shape at freestream velocities up to 150 m/s, the highest velocity used in their simulations. However, it is not obvious that this conclusion would also be applicable for WMS-2f measurements because the line shape differs significantly from that of a Voigt-shaped curve. Also, it is not known if the distortion-free assumption breaks down at sufficiently high velocities. Thus, one purpose of this study is to investigate a significantly nonuniform flowfield and evaluate its effect on the Doppler shift measurement of the resulting WMS-2f signals.

III. Nonuniform Flowfield Simulation

Figure 3a shows a simple case of a nonuniform flowfield. The central portion is plug flow at freestream velocity U_0, while the gas adjacent to the walls is stagnant with zero velocity. The plug flow section occupies 75% of the total path length, whereas the stagnant regions account for the remaining 25%. The temperature and pressure are assumed uniform at 296 K and 1 atm, respectively, and the oxygen mole fraction is set at 0.2062 (assuming 50% relative humidity). The simulated path length is 150 cm for each beam and the crossing angle is $2\theta = 90$ deg. Figure 3b shows the component of the velocity parallel to the beam, $U_\parallel$, as a function of location along the path for both beams. Within the plug flow section, $U_\parallel$ is equal to $U_0 \cdot \sin(45 \text{ deg})$, or $0.707U_0$. Figure 3b also shows the path-integrated numerical averages of $U_\parallel$ across both paths, $\bar{U}_\parallel = \pm 0.527U_0$. Using Eq. (1), the sensor would be expected to return a value of $U_{0,\text{meas}} = 2\bar{U}_\parallel/2 \sin\theta$, or $0.75U_0$, if stagnant space is not accounted for and if there is no error due to line shape distortion.

For the simulation, the path-integrated WMS-2f signal from each beam is calculated from the sum of the individual components along the path as a function of laser wavelength. For this example, there are two regions, the stagnant region and the plug flow region, each with slightly different Doppler-shifted line shapes. The resulting distorted WMS-2f line shape is then compared to the WMS-2f line shape generated from a uniform flow with the same path-averaged value of velocity to investigate the extent of distortion. These calculations were performed primarily for a modulation depth of $m = 1.9$ ($m \equiv a/\Gamma$), where a is the modulation amplitude (0.095 cm^{-1} in this case) of the diode laser and Γ the half-width of the pressure- and Doppler-broadened direct absorption line shape at half-maximum. The companion paper [1] described a method to identify the position of the WMS-2f line shape using 100 discrete points, and this scheme is evaluated using the distorted WMS-2f line shapes to determine the influence of the line shape distortion on the apparent Doppler shift. These simulations are performed at multiple values of U_0: 250, 500, and 1000 m/s. In addition, the ratio of the plug flow length to the total path is varied from 50 to 100%. Two cases at 75% plug flow with $U_0 = 250$ and 1000 m/s ($U_\parallel = 187.5$ and 750 m/s) are analyzed in detail as an example.

For the first case, $U_0 = 250$ m/s, with 75% plug flow and 25% of the path length in the stagnant gas, the distorted path-integrated WMS-2f line shape is compared to the line shape for a uniform (i.e., 100% plug flow) velocity component of 187.5 m/s along the entire path, and the differences between the two line shapes are an indicator for distortion produced by the nonuniformities. Figure 4a shows both the uniform and distorted (i.e., 75% plug flow) WMS-2f line shapes in the beam 1 direction, along with the residual between the two. The distorted line shape shown in the graph is the WMS-2f analog to the composite absorbance of Fig. 2b. The distortion is clearly very small, with the residual distortion reaching values which are ~3 orders of magnitude less than the line-center peak height. The fact that the residual is slightly positive on both sides of the line center indicates that the distorted WMS-2f waveform is slightly wider than the uniform WMS-2f, which would be expected based on the behavior seen in Fig. 2. The Doppler shift measurement from the distorted WMS-2f line shapes yields 187.8 m/s, which is within 0.3 m/s, or 0.15%, of the actual averaged value of 187.5 m/s, thus suggesting that the correct value of the plug flow velocity $U_{0,\text{corr}}$ can be obtained from this measurement by simply multiplying the measured velocity $U_{0,\text{meas}}$ by the path length ratio (also used by Allen et al. [7]).

$$U_{0,\text{corr}} = U_{0,\text{meas}} \frac{L_{\text{flow}} + L_{\text{stag}}}{L_{\text{flow}}} \tag{2}$$

The plug flow approximation used above produces a step function change in velocity, which is a "worst case" for practical flowfields that contain velocity gradients; for example, the velocity typically varies across a boundary layer from zero at the wall to the freestream velocity. In this case, there is a smooth variation in the Doppler-shifted line shape corresponding to the local value of velocity, which is a less severe distortion than the plug flow simulation described above, and the resulting error would be less than an equivalent plug flow profile with the same path-integrated average velocity. Because the maximum error observed for the plug flow approximation with a freestream velocity of 250 m/s is only 0.15%, a profile containing boundary layer velocity gradients would yield a measurement error

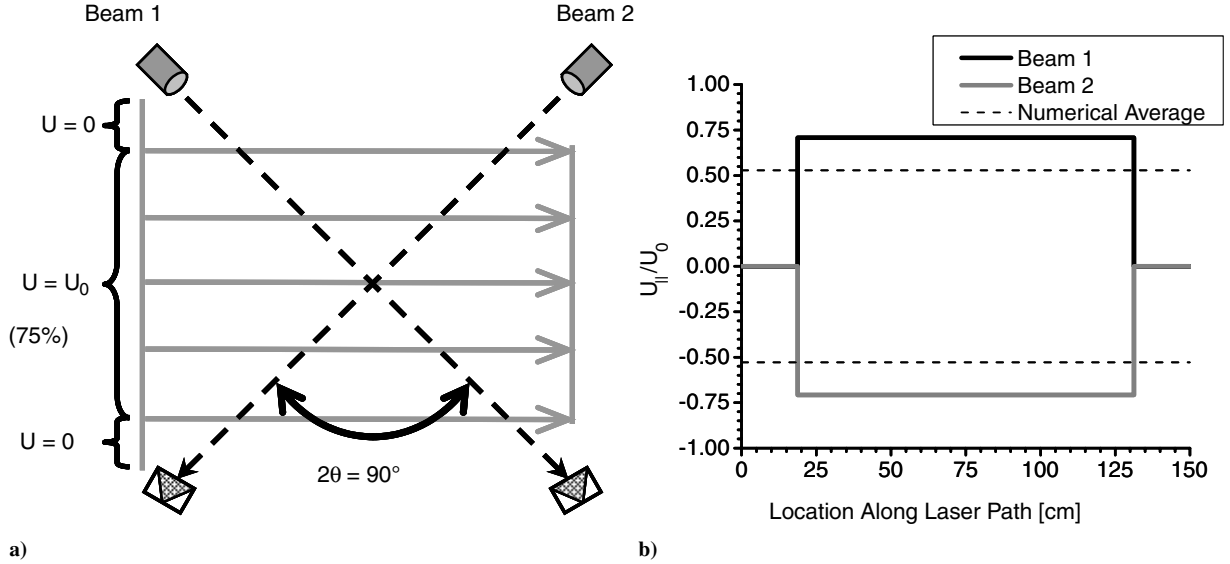

Fig. 3 a) Model for nonuniform flowfield simulation; b) resulting velocity profile normal to beam direction.

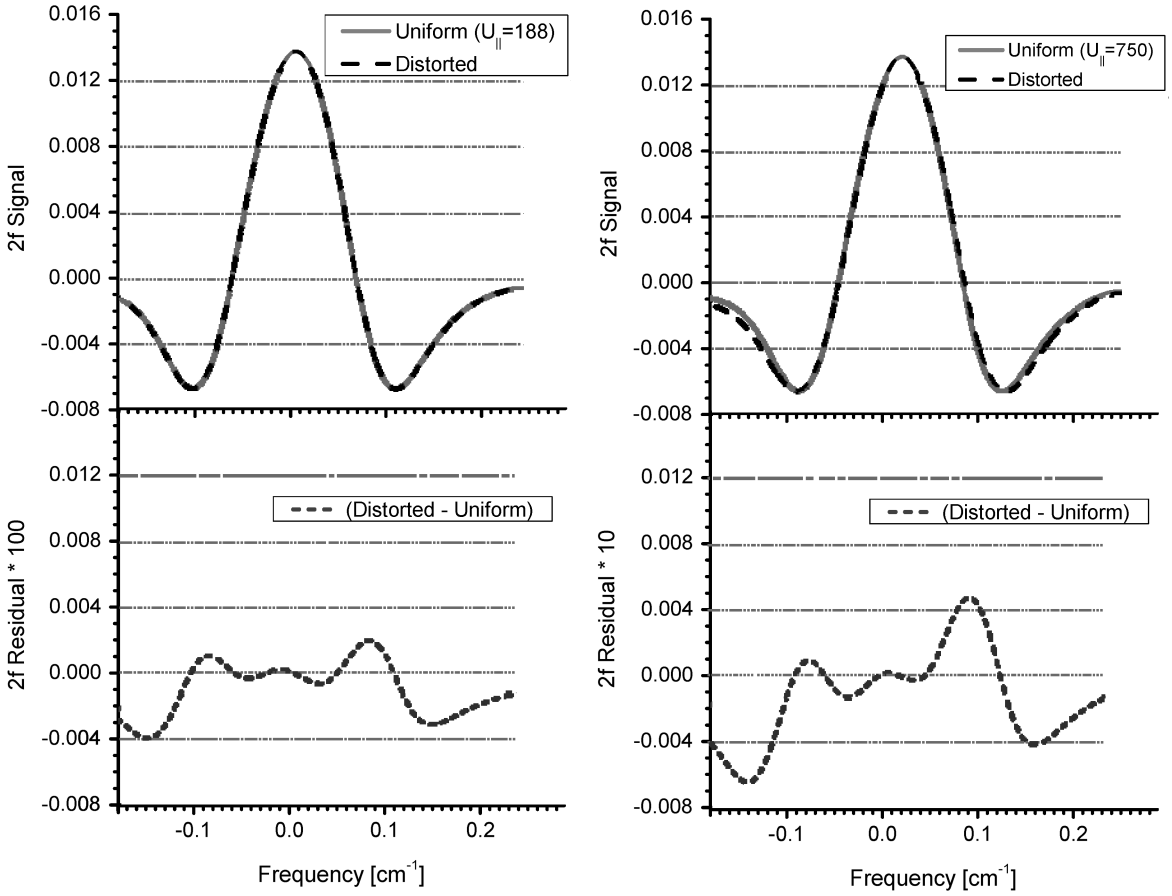

Fig. 4 Uniform and distorted WMS-2*f* line shapes from beam 1 path from Fig. 3, with residual between a uniform flow and a distorted flow with 25% stagnant and 75% uniform plug flow, for a) $U_0 = 250$ m/s and b) $U_0 = 1000$ m/s. (Note the modulation amplitude $a = 0.095$ cm^{-1} with a laser scan range of 0.423 cm^{-1}.)

less than 0.15%. Note that the resulting measured velocity will be a path-integrated value and will in general be less than the freestream velocity. This is not a problem for mass flux measurements, where the bulk-averaged velocity is the desired quantity, but an estimation of the freestream velocity will require characterization of a correction for the boundary layer portions of the optical path.

The simulation calculations show that WMS-2f line shape distortion is negligible at subsonic velocities relevant to the Pratt and Whitney aeroengine; however, supersonic gas velocities were also investigated. One such condition is shown in Fig. 4b where $U_0 = 1000$ m/s, which represents a Mach number of 2.9 at 296 K; this is a path-averaged mean velocity of 750 m/s for the 75% plug flow case, and the distorted WMS-2f waveform is compared with uniform flow in Fig. 4b. This case is essentially the WMS-2f version of the direct absorption line shapes shown in Fig. 2. The residuals from the line shape distortion are 1 order of magnitude greater than that for the subsonic $U_0 = 250$ m/s case. In addition, there is considerable asymmetry with respect to the line center, with the wider section shifted in the direction of larger velocity magnitudes (as seen in Fig. 4). Equation (2) gives a value for $U_{0,\text{corr}}$ of 1026 m/s, which is 2.6% higher than the freestream velocity. It is noteworthy that for both the 250 and 1000 m/s casess, the WMS-2f distortion appeared to be at a minimum at the feature's line center, and thus our numerical scheme for real-time determination of the position of the line shape is more sensitive to the distortion of the velocity nonuniformity than a measurement at the line center. The 100 point numerical scheme described earlier [1] is needed for subsonic velocities with Doppler shifts that are a small fraction of the absorption linewidth. For supersonic velocities with larger Doppler widths, this signal averaging scheme is not required, and these model results suggest other schemes to determine the position of the line shape is more appropriate and accurate for high velocity flows.

The simulations are summarized in Table 1 where the % error of the apparent velocity from the true velocity is given for $U_0 = 250$, 500, and 1000 m/s with plug flow fractions of 100, 90, 75, 60, and 50%. Note that fractional error for a given U_0 depends on the sensor crossing angle 2θ, and Table 1 gives the values for $2\theta = 90$ deg. The actual crossing angle in the beam path in the Pratt and Whitney aeroengine bell mouth was $2\theta = 37.7$ deg, and for this case it takes a larger value of U_0 before the errors from the plug flow correction become significant; for example, the results for 250 m/s at 90 deg are equivalent to 550 m/s at 37.7 deg (the errors for $2\theta = 37.7$ deg are also listed in Table 1).

The first conclusion that can be drawn from Table 1 is that at sufficiently low velocities, for example, $U_0 \leq 250$ m/s, the error introduced by flowfield-induced distortion is essentially negligible,

Table 1 Percent error of Doppler shift measurement from numerical path-averaged velocity

	100% Plug flow	90% Plug flow	75% Plug flow	60% Plug flow	50% Plug flow
$U_0 = \mathbf{250}$ **m/s**, $2\theta = 90$ deg (550 m/s, $2\theta = 37.7$ deg)	**0**%	**0.1**%	**0.2**%	**0.1**%	**0**%
$U_0 = \mathbf{500}$ **m/s**, $2\theta = 90$ deg (1100 m/s, $2\theta = 37.7$ deg)	**0**%	**0.4**%	**0.6**%	**0.4**%	**0**%
$U_0 = \mathbf{1000}$ **m/s**, $2\theta = 90°$ (2200 m/s, $2\theta = 37.7°$)	**0**%	**1.6**%	**2.6**%	**1.7**%	**0**%

and Eq. (2) can be used to account for nonuniformities in velocity; note that this covers all velocity ranges measured in the Pratt and Whitney aeroengine.

At higher values of the freestream velocity, the error can become more severe and is highly dependent upon the specific properties of the flow. For example, at $U_0 = 1000$ m/s, the error is almost negligible for a 50/50 split between plug flow and stagnant regions. This is not surprising, because the sum of the two equal line shapes should merely be a widened line shape centered between the two, with no asymmetry. By contrast, the error for 75% plug flow is 2.6%, as described previously. Thus, for supersonic flowfields the interpretation of the data may require a more sophisticated correction than Eq. (2).

All of the WMS-2f simulations performed in the above analysis used a modulation index m of 1.8, which is the same index used in our aeroengine measurement campaign and provides the maximum WMS-2f signal strength. However, it is worth discussing the effects of changing m. If m is reduced, the distortion of the WMS-2f line shape by velocity nonuniformities is increased (e.g., for $m = 0.5$, the 250 m/s plug flow example produces a line shape that is 0.46% wider than the line shape for a uniform flow at 187.5 m/s; for $m = 1.8$, the change in width is only 0.04%) Thus, the use of smaller m can aid the investigation of velocity nonuniformities. Larger m begins to include contributions from neighboring lines and was not investigated further.

IV. Density Nonuniformities

The analysis of density nonuniformities is similar to that of velocity, in that the measurement reflects the path-averaged value. A typical example would be a case in which the sensor is measuring the velocity and density of gas in the throat of a test section which experiences compressibility effects, such as the realistic bell mouth shown in Fig. 5. At sufficiently high throat Mach numbers, such as $M > 0.3$, the local density in the throat will be lower than ambient. Outside of the test section, there are stagnant air paths near the transmitting and receiving optics which might not be purged, as was shown in Fig. 1. In those regions, the ambient density will be higher than that in the throat. Both sections will contribute to the overall density as measured by the sensor, which, as was the case of the velocity at low distortion conditions, will reflect the numerically averaged density across the path. Specifically, the measured density for this case can be expressed as

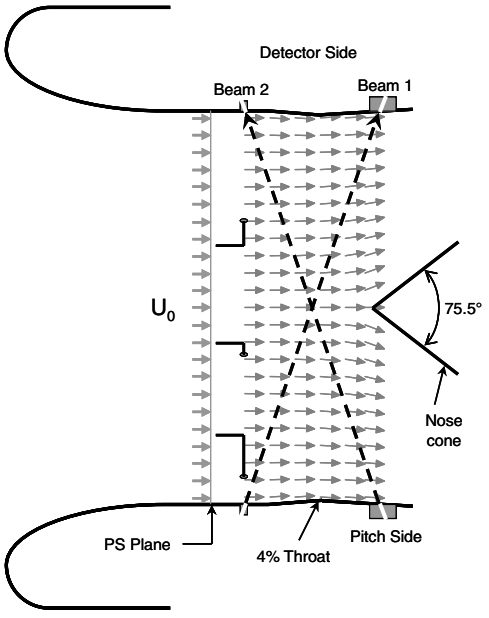

Fig. 5 Schematic showing velocity vector variation through bell mouth as a result of throat and fan nose cone.

$$\rho_{\text{meas}} = \rho_0 \frac{L_{\text{stag}}}{L_{\text{total}}} + \rho_t \frac{L_{\text{flow}}}{L_{\text{total}}} \tag{3}$$

where ρ_0 is the ambient density and ρ_t is the density in the throat. Equation (3) can be rearranged to obtain ρ_t from the sensor-measured density ρ_{meas}, assuming that ρ_0 is known by independent means:

$$\rho_t = \frac{L_{\text{total}}\rho_{\text{meas}} - L_{\text{stag}}\rho_0}{L_{\text{flow}}} \tag{4}$$

Equations (3) and (4) are valid for optically thin cases with total absorbance less than 10%. The measured absorbance in our aeroengine tests is ~4%.

V. Nonuniform Flow Model for Aeroengine Bell Mouth

The mass flux sensor was built into a bell mouth immediately upstream of the turbofan, with an effective beam crossing angle of $2\theta = 37.7$ deg. This bell mouth geometry contributed to a nonuniform velocity profile within the sensor measurement region. Specifically, there was the presence of a throat with 4% area reduction, and the fan nose cone which protruded forward about 13.5 cm into the bell mouth, as displayed in Fig. 5. These two components affect the flowfield in two significant ways as follows:

1) Assuming incompressible flow, the throat area reduction accelerates the bulk axial velocity by as much as 4.2%.

2) A radial component to the local velocity vectors is introduced by the cone, and to a lesser extent the throat, which generates flow deflection, as shown in Fig. 5. It is important to emphasize that this flow diversion begins significantly upstream of the geometric body, which illustrates that the relatively small intrusion of the cone into the measurement region can induce a significant change in flow direction well upstream of the cone tip. This flow diversion changes the angle between the laser beam and the local velocity vector, which in turn alters the local contribution to the Doppler shift. To illustrate the sensitivity of the velocity measurement to the beam/velocity vector angle, consider that for a crossing angle of $2\theta = 37.7$ deg, a 1 deg change in the angle between the velocity vector and the laser beam will result in a 5% change in the value of the Doppler shift (at $2\theta = 90$ deg, the corresponding change is 1.7%).

Thus, if left uncorrected, velocity nonuniformities can lead to significant measurement error.

In addition to the physical flow perturbations due to the intake area change of the throat and the diversion of the flow by the nose cone, the boundary layers can influence the flow measurement in two ways: first, boundary layers produce a stagnant region near the walls where the velocity is reduced, and second, these boundary layers grow with axial distance. This produces a change in the effective area of the core region and an acceleration of the freestream velocity. To account for these sources of nonuniformities, we developed a flow model to approximate the actual flowfield of the bell mouth within the measurement region, and used the results from this model to correlate the velocity value measured by the sensor with the uniform axial velocity at the pitot-static (PS) plane, U_0. The model consists of the following key elements:

1) The model is functionally incompressible, as compressibility effects are ignored within the measurement region; that is, density is assumed constant.

2) The axial component of the core velocity is assumed to be uniform across the duct and is determined from conservation of mass based on area change, including the area change caused by boundary layer growth.

3) The throat and cone are approximated using potential flow solutions for a 2-D corner, which are modified to simulate the effect of axisymmetry. The solutions provide the angle of the local velocity vector.

4) Boundary layer growth is modeled based on measurements made by Pratt and Whitney, assuming a growth rate with flow distance to the 6/7 power ($x^{6/7}$) for turbulent flow [8].

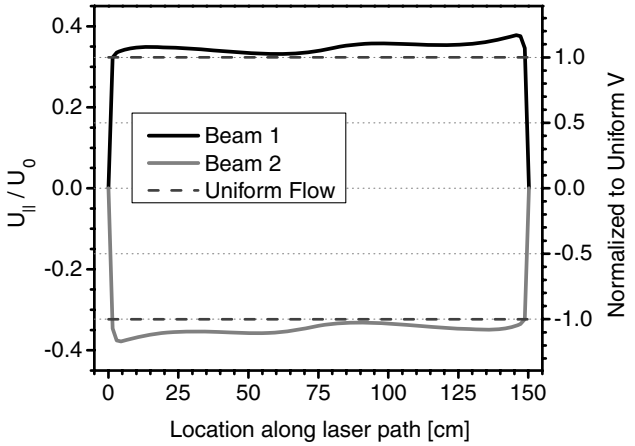

Fig. 6 Component of the local velocity vector from flow model parallel to the laser beam as a function of location along the beam.

Once the solution to the flow model is obtained, the mean velocity measurements are calculated along one of the laser paths; the corrections for the second beam path are known by similarity. The path is divided into small subsegments, and the component of the local velocity vector parallel to the beam $U_{\|}$ is calculated at each segment from the dot product of the velocity vector and the beam normal vector. The resulting velocity profile is then numerically averaged and compared to the measurement that would be obtained assuming uniform, boundary layer-free axial flow at the PS plane, which at $2\theta = 37.7$ deg corresponds to $U_0 \sin\theta = 0.323 \cdot U_0$. Note that WMS-2$f$ simulations are not required for this calculation, because the distortion effects of the WMS-2f line shape from nonuniformities are negligible at subsonic velocities.

Figure 6 displays the results of the flow model calculations using a Pratt and Whitney computational fluid dynamics (CFD) calculation of the flow (includes a boundary layer over approximately 2.2% of the path on either side of the bell mouth), showing the profiles of the local velocity vector parallel to the laser beam normalized by the uniform flow velocity at the PS plane, $U_{\|}/U_0$, for both beams 1 and 2. Also shown is the corresponding value assuming uniform flow, $0.323 \cdot U_0$. The largest value of the local velocity occurs at the downstream closest to the nose cone, where the maximum deviation of the local velocity from the uniform flow value is 17%. There is also a slight increase on the upstream side due to deflection and acceleration from the contracting throat, which is up to 8% larger than the uniform flow value. Overall, the apparent path-integrated velocity value measured by the sensor is 6.6% larger than the uniform flow value. Because the solution of the flow model does not depend on U_0, this correction factor can be used for any measurement made by the sensor in the absence of compressibility effects.

When compressibility effects are included, the contraction at the throat causes the static density to decrease, which increases the local velocity beyond its incompressible value. As a consequence, both velocity and density must be modeled across the path to obtain their path-averaged values as measured by the sensor. An interesting artifact of the compressibility corrections is that the mass flow results are essentially the same with or without compressibility. On a basic level this makes sense: adding compressibility means that both velocity and density will be adjusted, and to obey conservation of mass, the product must remain unchanged after the correction. There is one complicating factor with this particular observation, in that the velocity correction includes the influence of a variable radial component, while the density is a scalar and thus has no such component. However, this effect is not significant for the crossing angle and velocity range in the aeroengine measurements.

VI. Aeroengine Measurement Campaign at Pratt and Whitney

The mass flux sensor was installed into the instrumentation bell mouth directly upstream of a turbofan engine at the Pratt and Whitney's aeroengine ground-test facility in East Hartford, Connecticut. The testing took place during 11–12 July 2005 in concert with the engine's final performance evaluation before certification. Although diode-laser-based mass-flux tests have been performed on an aeroengine in the past, specifically the Pratt and Whitney F100 military turbofan [6], this was the first known test of such a sensor with real-time capability. The engine is a midsized commercial turbofan developed for the 100-passenger Airbus A318 and is capable of a maximum thrust of 24,000 lb at takeoff with an inlet air velocity of 175 m/s (390 mph). The engine officially entered the commercial market on 17 August 2005.

The testing facility at East Hartford consisted of a test cell built into an enclosed hangar. The engine was mounted from an overhead brace, and the air ingested by the engine was drawn from outside of the building through a large-area louvered filtration system. This air passed by a large burner array approximately 15 m upstream of the engine. These burners can provide an elevated inlet temperature of 130°F (54°C) for hot performance tests. The engine itself had an instrumented fiberglass bell mouth mounted just upstream of the fan. The bell mouth provides a well-characterized, uniform flowfield into the engine, which allows the eight PS pressure probes to obtain accurate measurements for the standard mass flow calculations. Figure 7 includes a photograph of a typical ground-test engine

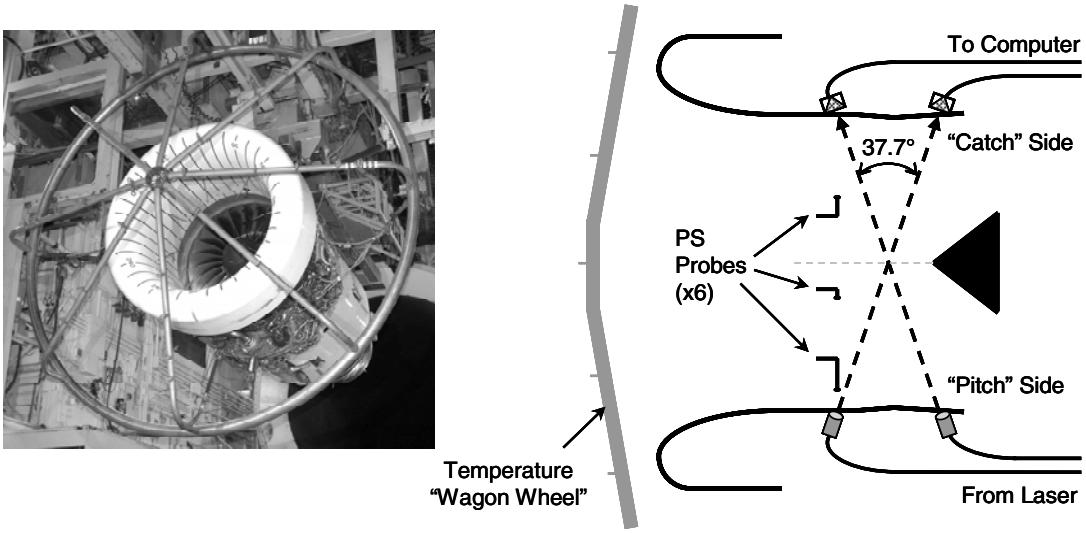

Fig. 7 Photograph of typical engine test-stand installation with instrumentation for inlet mass flux (left). Schematic of laser sensor installation in bell mouth (right).

mounting with the instrumentation to monitor mass flow, and a cutaway schematic of the bell mouth with the sensor mounting. Note the engine photo shows the large ring-and-spoke "wagon wheel," which was instrumented to measure temperature at multiple locations across the inlet area of the bell mouth. The total length of the bell mouth was 147 cm, and the diameter was 144 cm at the PS measurement plane. A throat with a 4% area reduction was located 38 cm downstream of the PS plane, and the fan nose cone protruded forward about 13.5 cm through the outlet of the bell mouth.

The mass flow through the engine is calculated from the data obtained using the eight pitot-static pressure probes and the temperature measurements from the wagon wheel. Because there is a Mach number difference between the temperature and pressure measurement locations owing to the converging flow area entering into the bell mouth, a flow model [9] is used to correlate the measured temperatures to the static temperature PS plane to calculate the mass flow. The model also includes the effect of the boundary layers, which had been well characterized from previous tests. The temperature and pressure measurements are averaged across all locations and over the measurement time, generally in the range of 2–5 min for a steady-state condition. The resulting time-averaged mass flow measurements have been shown to have an absolute uncertainty of $\pm 0.5\%$ [9], making them an excellent reference for the diode-laser sensor measurements reported here. One caveat of the test-stand instrumentation involves the difficulties during rainy weather when the saturated air tends to condense inside the bell mouth (due to the drop in static temperature and pressure) and liquid water plugs the pressure probes. Our diode-laser sensor was not thwarted by these conditions, although a correction for the water content is required. Throughout all testing, the humidity of the ambient air was monitored by standard test-cell instrumentation. The ambient H_2O molar concentration was generally in the 1.96–2.15% range, resulting in an oxygen concentration of 20.50–20.54%. Both the oxygen mole fraction and the contribution of the water vapor to the mixture molecular gas constant are accounted for in the sensor-based calculations of the air density.

VII. Sensor Incorporation into the Bell Mouth

The transmitting ("pitch") and receiving ("catch") optics were built into existing bell mouth instrumentation bosses. One set of pitch and catch optics were mounted in the forward PS bosses, replacing two of the PS pressure probes and thus reducing the pressure measurement from 8 to 6 points. The other set of pitch and catch optics were mounted in the aft boundary layer (BL) bosses, which were located 48.6 cm downstream of the PS bosses and were otherwise unused throughout the duration of testing. The geometry of the bosses resulted in an effective crossing angle of $2\theta = 37.7$ deg and a beam path length of 150.5 cm from the PS boss to the BL boss on the opposite side.

The pitching mounts each consisted of a fiber pitching lens attached to a multi-axis stage which allows for precise beam alignment. Each beam passed through a 1.6 cm diam fused silica window which is AR coated for 760 nm and has a 1 deg wedged face. Each of the catching mounts on the opposite side consisted of a 25.4 mm f.l. spherical mirror and a photodetector. The beam received by these optics passed through another AR-coated window which has a 3 deg wedge angle—the wedged windows prevent interferences of the wavelength-tuned laser beam from etalons formed by the window surfaces. The paths outside of the bell mouth (27.2 cm) were not purged or enclosed, and their contributions to the velocity and density measurements were mitigated using Eqs. (2) and (4), respectively.

Some further discussion of the fastening of the optical hardware is warranted. The engine bell mouth is a strongly vibrating environment, where displacements on the order of 1 cm at a frequency of several hundred Hz are observed. To make safe, successful measurements, we needed to ensure that all attachments were vibration proof. Several strategies were employed to that end. All bolts and locknuts used thread-locking compound, and included covers with through holes which allowed the fasteners to be tied down with safety wire to anchor them together and prevent them from becoming foreign object debris (FOD). As an added measure, epoxy was added to the surface interface of all mating parts to add strength. As a result of these measures, no failure of the fastening components was observed throughout the entire test campaign. It is therefore presumed that this scheme could also be successfully applied to other similarly harsh measurement environments.

A fiber-coupled distributed feedback (DFB) laser replaced the vertical cavity surface emitting laser (VCSEL) used in our previous work [1] providing a 15-fold increase in laser power and removing the need to fiber couple a free-space laser at the test stand. In addition, the sensor software was updated for real-time operation with simultaneous data input and data processing (in the previous version, these processes were sequential) and the laser scanning rate was increased from 50 to 100 Hz. The alternation between direct absorption density measurements and WMS-2f velocity measurements enabled averages of 50 scans across the absorption feature with a 1 Hz measurement rate.

VIII. Results and Discussion of First Test Run

The 1 Hz real-time results of test 1 are displayed in Fig. 8, with the velocity and density corrected to the PS plane using the compressible version of the flow model. The density data have been postprocessed to provide an average over a 10-s cycle for comparison with the Pratt and Whitney-measured velocity and density for each steady-state condition. In the segment of the test shown in Fig. 8, the sensor velocity consistently matches the Pratt and Whitney velocity to within approximately 1 m/s, and the 1-s standard deviation of the instantaneous velocity relative to the mean measured value is 1.24 m/s. Note that the sensor appears to capture some transient velocity behavior, such as the period between 17 and 20 min where there are visible decays in the nominal 60 m/s and 65 m/s velocities, not observable with the standard Pratt and Whitney instrumentation. The optical-sensor data shown in Fig. 8 were compromised somewhat by the performance of one of the optical mounts, and future designs should permit improved velocity accuracy.

The density measurements show significant scatter, even after 10-s averaging. Unfortunately, one of the optical mounts was not sufficiently rigid, and the scatter in the data is likely dominated by the consequences of this compromised mechanical component. Subsequent runs with a temporary field fix provided some mitigation with scatter in density data significantly smaller than that in Fig. 8; hence we expect an improved mounting design could result in better signal-to-noise ratio (SNR) than shown in Fig. 8. The region between 27 and 29 min in Fig. 8 is especially problematic, where the engine vibration produced a mechanical resonance in this optical mount that corrupted the signal to such a degree that an accurate measurement was not possible. If this noisy condition is

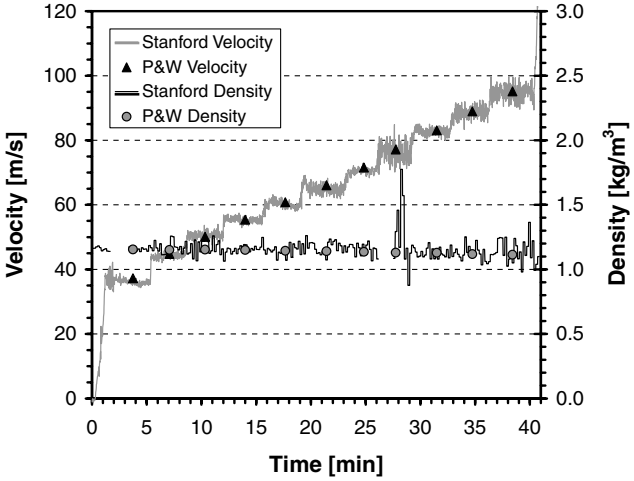

Fig. 8 Real-time velocity (1 s) and density (10 s) measurements from a typical test. ($2\theta = 37.7$ deg).

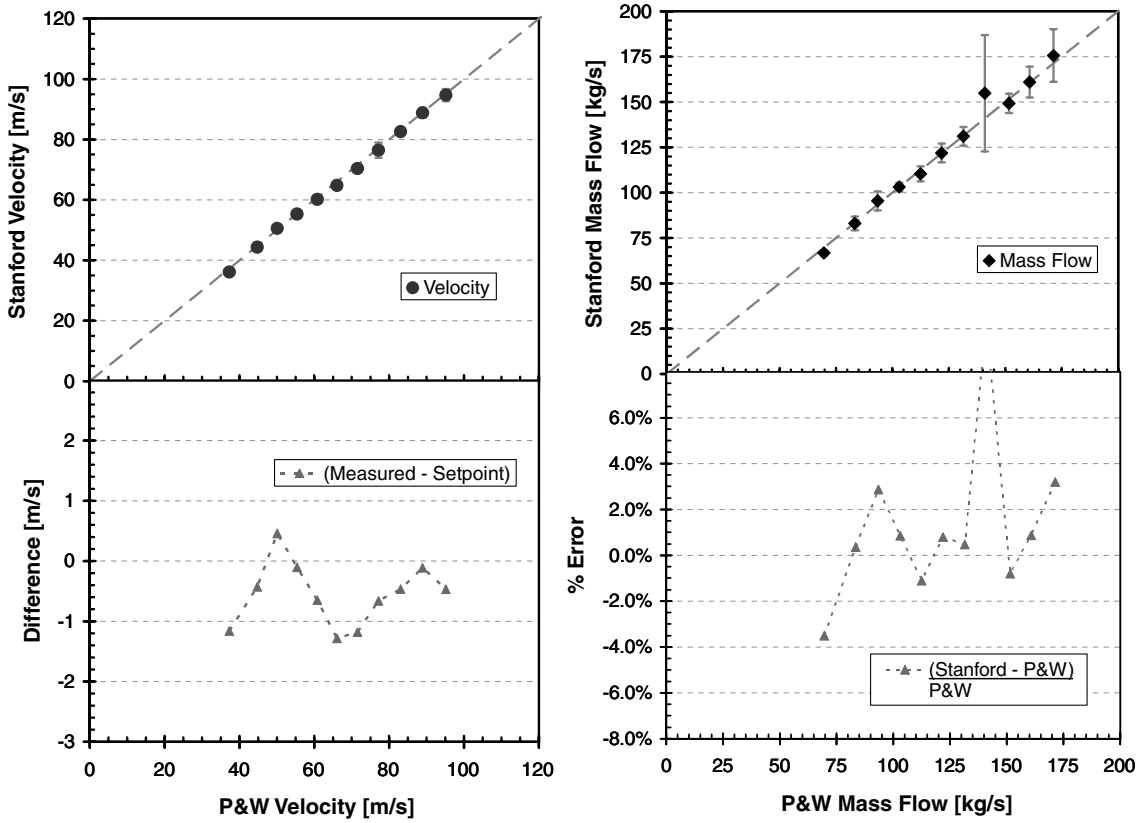

Fig. 9 Comparison of optical-sensor, time-averaged (10 s) measurements to Pratt and Whitney measurements for data from Fig. 8 for a) velocity and b) mass flow. Differences are also shown ($2\theta = 37.7$ deg).

neglected, then the sensor-measured density agrees with the Pratt and Whitney density to within 1.1% on average, with the greatest single deviation being 2.9%. The standard deviation of the instantaneous (i.e., 10 s) density relative to the mean measured value is 4.1%. These results highlight the noise sensitivity of direct absorption measurements compared to WMS-2f measurements. The velocity measurements also include data from the faulty laser path, yet the high-frequency filtering inherent in WMS-2f sifts out much of the noise. Thus, it is evident that a less noise-sensitive density measurement method is desired, potentially using a WMS-based strategy.

Figure 9 shows the time-averaged velocity a) and mass flow b) versus the Pratt and Whitney-measured values for the test 1 data from Fig. 8, along with the corresponding differences between the sensor and Pratt and Whitney measurements. The total averaging time for each data point is approximately 3 min corresponding to the Pratt and Whitney measurement method [2,9]. The averaged mass flow values are calculated from

$$\bar{\dot{m}}_{\text{meas}} = \frac{\sum_{n=i}^{i+N-1} U_{\text{meas}}(t_n)\rho_{\text{meas}}(t_n)A_{\text{tunnel}}}{N} \tag{5}$$

For the velocity in Fig. 9a, the mean difference between the sensor and Pratt and Whitney velocities is 0.63 m/s. The wind-tunnel tests described in a previous paper [1] found an average difference of 0.25 m/s, and the ratio of 2.5 between the scatter of the engine and wind-tunnel measurements is roughly equal to the ratio of sensitivity (2.2) because of the different crossing angles ($2\theta = 90$ deg in the wind tunnel and 37.7 deg in the engine). The data point at 141 kg/s is neglected here, as it was taken with the vibrating optical mount. The average difference between the optical sensor and Pratt and Whitney-measured mass flow is 1.3%. It should be stressed that the quality of the density measurement is the primary limiting factor in the accuracy of the mass flow. Later in this paper, we will estimate the potential mass flow accuracy for this sensor using the best data selected from multiple runs. It is also important to note that the measurements reported in this paper are from a single ground-test measurement campaign. It is quite likely that the lessons learned here would lead to improved optomechanical design for future tests.

IX. Summary of Test Results

In addition to the first test run, four additional data sets were collected, with two of these runs conducted at an elevated inlet temperature of 130°F. Because of the deteriorating performance of the previously identified loose optical mount, the instantaneous velocity measurements degraded with total run time with standard deviations as much as 5 times larger. However, the density measurements were improved by acquiring density data only from the beam path without the faulty mount. The 10-s standard deviation of density is reduced by approximately a factor of 3, and the difference from the test-cell standard decreases by at least a factor of 2.

Figure 10 shows the velocity a) and mass flow b) for all of the test runs averaged over 3 min for direct comparison with the traditional measurements. The error bars indicate the 1-s standard deviation at each condition to illustrate the spread of the measurements at the tunable diode-laser (TDL) sensor bandwidth. The velocity results in Fig. 10 show remarkable agreement with the calibration values from the standard probe instrumentation. Many of the values are within ±1 m/s, and the overall mean agreement is 0.67 m/s. The mass flow results display more scatter, though this would be expected at low velocity conditions in which the velocity uncertainty dominates measurement accuracy. However, the relatively high percentage difference at the highest flow rates, that is, above 250 kg/s, is somewhat surprising, and is almost certainly attributable to errors in the density measurement. Again, this highlights the vulnerability of the direct absorption measurements to mechanical noise, particularly during the highly vibrating takeoff conditions like those shown at 295 kg/s. Measurements at an inlet mass flow rate of 150 kg/s

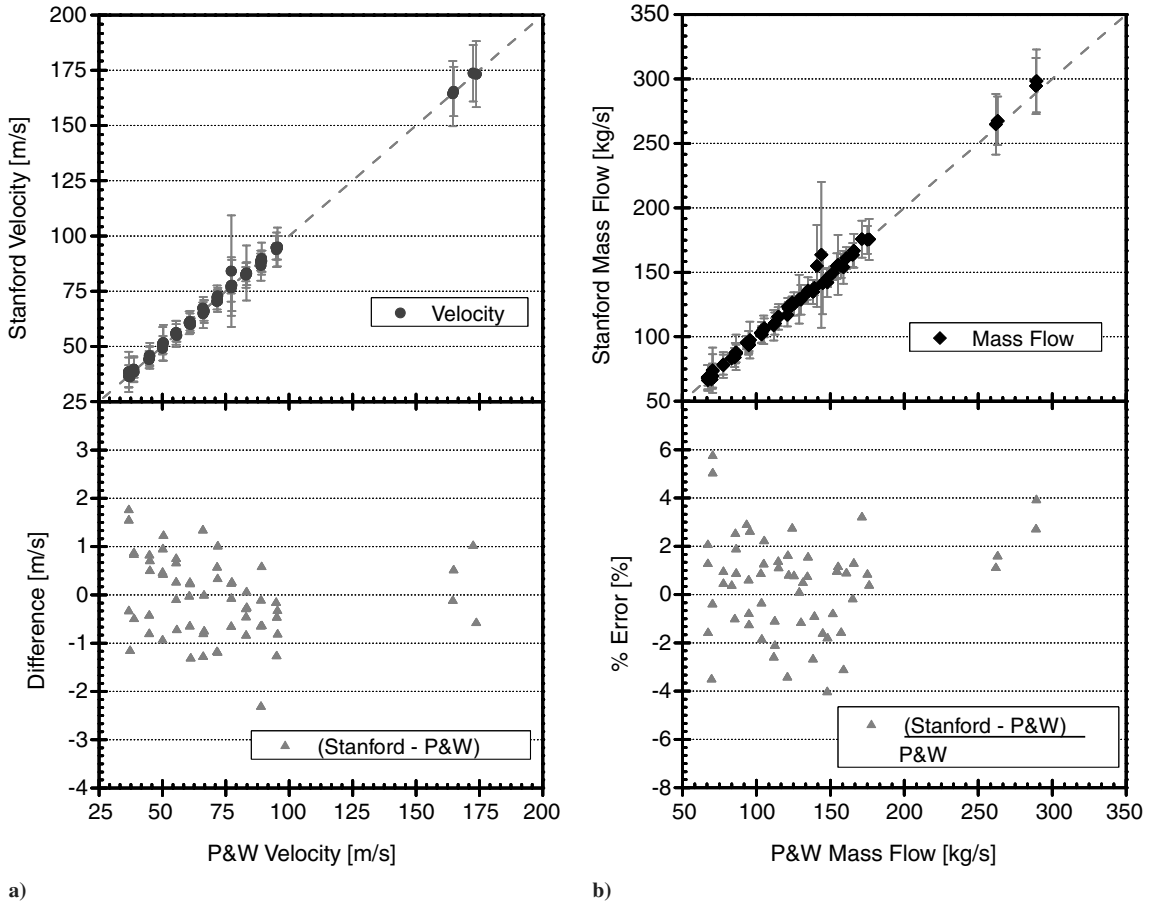

Fig. 10 Comparison of optical-sensor, time-averaged (3 min) measurements to Pratt and Whitney measurements for all data taken during test campaign for a) velocity and b) mass flow. Differences are also shown ($2\theta = 37.7$ deg).

correspond to engine conditions similar to those shown in Fig. 8 between 27 and 29 min, and thus we consider the 10% error in the inferred mass flow rates near 150 kg/s to be an anomaly caused by the problematic vibrating mount. Overall, the average difference between the sensor and Pratt and Whitney mass flux is 1.5%. Table 2 summarizes the measurement results from these tests, highlighting the highest quality velocity and density values as well as the overall averages; note the 1 Hz standard deviation of the mass flux data is artificially large due to the vibrating optical mount.

The measurements reported here were the results of a single measurement campaign in the aeroengine test facility conducted over three days. Thus, we were unable to improve the mounting design beyond simple field repairs during short periods of access to the test bay. Our best velocity performance occurred early in the tests and degraded with the failure of one optical mount. The density measurements are made on only one of the two optical paths, and the data quality improved throughout the campaign as we improved optical alignment, real-time analysis software, and incorporated other lessons learned. If we consider the direct absorption density measurements and the WMS-2f velocity measurements to be independent determinations, it is appropriate to investigate the potential best-case accuracy of the sensor given the highest quality data sets in Table 2, by choosing the best velocity results and the best density results from different runs. The definition $\varepsilon_{\%,1\,\mathrm{s}}$ of the instantaneous 1 Hz mass flow uncertainty was given in Eq. (14) of [1]. The error analysis in [1] assumes that there is no persistent bias error source and is based on the root sum square of the time-averaged percent error $\varepsilon_{\%,\mathrm{ave}}$ and the 1-s percent standard deviation $\sigma_{\%}$: The uncertainties can be separately evaluated for the density and the velocity, and because the velocity range in the best velocity run is limited to 37–95 m/s, the same restriction is placed on the best density run data. From these data, the time-averaged and instantaneous mass flow accuracies can be calculated using the root sum square of the velocity and density uncertainties at a given velocity U.

This analysis is only valid if the error sources are free of any source of persistent bias, meaning that they are random, normal, and uncorrelated. It is reasonable to ask whether the mass flow data presented here obey this classification. Figure 11 shows histograms for the time-averaged errors for a) velocity and b) mass flow from the

Table 2 Summary of mass flux sensor measurements in Pratt and Whitney aeroengine

	Velocity	Density	Mass flow
Best test run—velocity measurements:			
Overall average difference from P&W	**0.63** m/s		
Overall standard deviation (1 s)	**1.24** m/s		
Best test run—density measurements:			
Overall average difference from P&W		**0.46**%	
Overall standard deviation (10 s)		**1.06**%	
Total—all tests			
Overall average difference from P&W	0.67 m/s	0.72%	1.5%
Overall standard deviation (1 s)	5.4 m/s	1.85%	10.2 kg/s

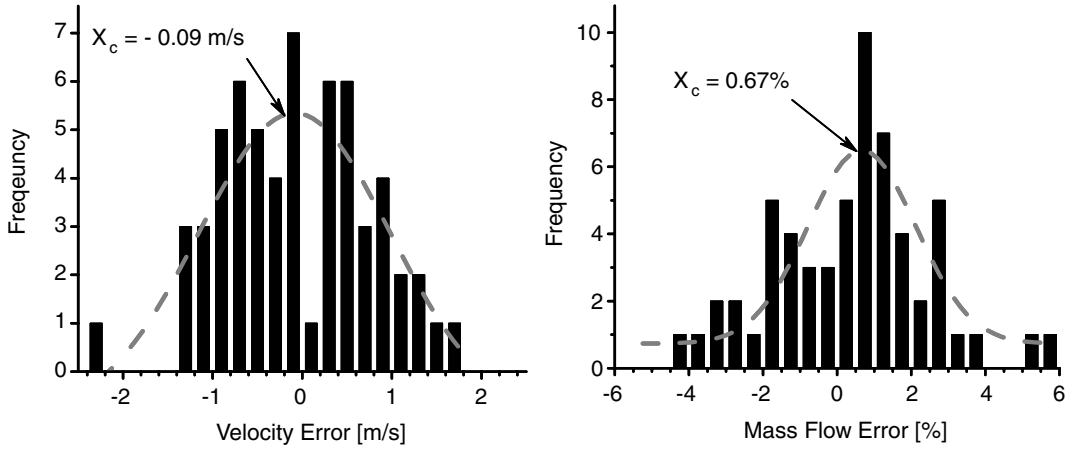

a) b)

Fig. 11 Histogram of time-averaged errors for a) velocity and b) mass flow from the data shown in Fig. 10. Best-fit Gaussian curves also included ($2\theta = 37.7$ deg).

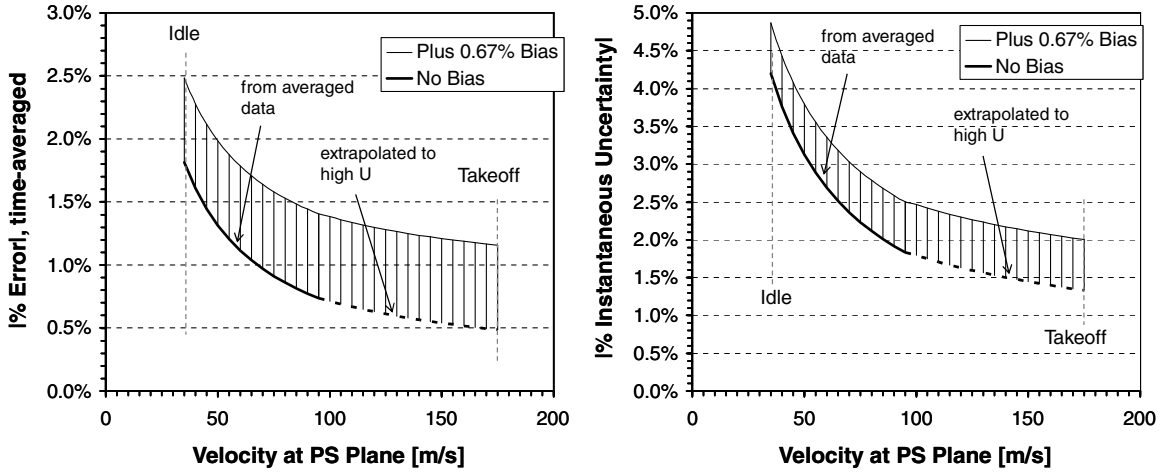

a) b)

Fig. 12 Predicted best-case mass flow a) time-averaged percent error and b) percent instantaneous uncertainty based on Table 3, including effect of potential 0.67% bias (1-s U, 10-s ρ).

data shown in Fig. 10. Both histograms include a best-fit Gaussian curve. In both cases, the data are roughly Gaussian in shape, with both datasets yielding a best-fit R^2 parameter of 0.67. The velocity data show a slight offset of -0.09 m/s, but even at the lowest observed velocity of 35 m/s this represents only 0.2%. At higher velocities, the bias is essentially negligible. A similar analysis performed on the time-averaged density (not plotted here) returned a bias of only 0.02%. However, the situation is somewhat different for mass flow, in which a bias of 0.67% is found. This suggests that the velocity and density errors are not entirely uncorrelated and evaluation of the mass flow sensor performance must include this bias to separate analysis of the density and velocity data.

The results of these mass flow uncertainty evaluations using separate data sets for velocity and density are shown in Fig. 12. Without the bias, the solid black curves illustrate the estimated performance for 1 Hz and time-averaged (3 min) measurements for the 37–95 m/s velocity range using the data in Table 2, and the dotted line extrapolates this performance to higher velocities assuming that increased noise does not become a limiting factor. The addition of the bias is shown by the upper bound curve in Fig. 12. The time-averaged (3 min) mass flow performance predictions in Fig. 12a are within 0.71% of the Pratt and Whitney values without bias for a velocity of 100 m/s and 1.38% including the 0.67% bias. The corresponding instantaneous (1 Hz sensor bandwidth) uncertainties are expected to be 1.8% at 100 m/s (2.47% including bias), with values as low as 1.35% (2.02% with bias) at higher velocities.

Miller et al. [6] quoted best-case mass flow accuracies in the 1–2% range and predicted accuracies of 3–4% for a sensor operated at 1 Hz. However, it must be remembered that their crossing angle was 90 deg, which provides 2.2 times greater velocity resolution. For this measurement campaign, we were limited to mounting the sensor in existing ports of the bell mouth, which limited the crossing angle $2\theta = 37.7$ deg; if the optimum crossing angle $2\theta = 90$ deg had been used, we estimate an increase in sensitivity of 2.2. If we can assume that the velocity uncertainties in Table 2 are directly proportional to the velocity sensitivity, then they can be scaled accordingly to account for a more favorable crossing angle. Table 3 shows how these best-case predictions at 37.7 and 90 deg calculated at a velocity of 100 m/s compare with the results of Miller et al. [6]. The values shown in parentheses include an additional 0.67% bias. The sensor reported here shows significantly greater accuracy than that of Miller et al. [6], most likely resulting from the superior precision of the WMS-2f-based velocity measurement, even in the face of added challenges such as a smaller beam crossing angle and considerable flowfield nonuniformity. Further development could lead to still better performance, which makes the oxygen absorption-based mass flux sensor increasingly viable for real-world aeroengine measurements.

X. Conclusions and Future Work

A real-time diode-laser-based sensor was developed to measure mass flux of an aeroengine inlet, via velocity and density, at a rate of

Table 3 Comparison of best-case mass flow prediction accuracies at 100 m/s compared to the results of Miller et al. [6]

	Sensor, 37.7 deg	Sensor, 90 deg	Miller et al. [6]
1 Hz	1.8% (2.47%)	1.25% (1.92%)	3–4% (predicted)
Long-term average	0.71% (1.38%)	0.44% (1.11%)	1–2%

1 Hz. The velocity is obtained from WMS-2f measurements of the Doppler frequency shift between an absorption feature of oxygen using two crossed beams through a flowfield, and the density is determined from a direct absorption measurement of integrated absorbance.

The issue of nonuniform flowfields was investigated using a simple model which simulates the distortion of WMS-2f line shapes caused by a velocity profile consisting of stagnant and plug flow regions. The simulations show that distortions to the WMS-2f line shapes are minimal at subsonic velocities, and that the measured frequency shift faithfully represents the numerically averaged velocity across the measurement path. A more detailed nonuniform flow model was developed for the Pratt and Whitney aeroengine bell mouth in ground testing. The model uses potential flow approximations to describe the velocity profiles within the sensor measurement section and correlates the velocity value reported by the sensor to the uniform axial velocity measured by the pitot-static pressure probes.

The sensor was installed in the aeroengine bell mouth for the ground test at Pratt and Whitney and successfully measured mass flow at a variety of conditions. We predict that the sensor is capable of measuring the time-averaged mass flow to within 0.71% (or 1.38% with an assumed 0.67% bias error) of the Pratt and Whitney value at a velocity of 100 m/s.

We recommend the following improvements to the sensor and its implementation:

1) Use the superior noise rejection of WMS-2f absorption measurements for the density determination.

2) Increase the acceptance solid angle and use more vibration-tolerant optical mounts.

3) Enclose the optical path outside the bell mouth to enable purging of the stagnant region, eliminate stray air currents, and protect from interference from other test-stand instrumentation.

4) Perform a simultaneous measurement of water vapor to account for variable humidity.

5) Shift the modulation frequency to higher values for improved noise rejection.

6) Simulate flow inlet distortions in advance to allow rapid corrections to the measured data. This is an important consideration since in-flight distortions of the inlet flowfield provide a significant challenge for conventional pitot and temperature probe-based instrumentation.

The successful operation of the engine inlet mass flux sensor opens the possibility for velocity and density measurements in other applications.

Acknowledgments

This research was supported by Pratt and Whitney. We wish to thank the people at Pratt and Whitney who helped us with engine mounting designs and ground testing, including Mark Jesse, Joseph Latour, Bruce Espinosa, John Roberts, Mike Pfeiffer, and McKen Mai.

References

[1] Lyle, K. H., Jeffries, J. B., and Hanson, R. K., "Diode-Laser Sensor for Air-Mass Flux 1: Design and Wind-Tunnel Validation," *AIAA Journal*, Vol. 45, No. 9, 2007, pp. 2204–2212.

[2] Abernethy, R. B., Roberts, J., Adams, G., and Steurer, J., "In-Flight Thrust Determination," SAE AIR 1703, Report of SAE Committee E-33, Society of Automotive Engineers, 1986.

[3] Williams, J. G., Steenken, W. G., and Yuhas, A. J., "Estimating Engine Airflow in Gas-Turbine Powered Aircraft with Clean and Distorted Inlet Flows," NASA CR-198052, 1996.

[4] Roberts, J. H., Beyerly, W. R., Mason, M. W., Glazier, J. R., and Wiley, R. H., "PW4084 Engine Testing in Altitude & Sea Level Test Facilities," *SAE Aerotechnology 1994*, SAE 94-2140, Oct. 1994.

[5] Schmid, N. R., Leinhos, D. C., and Fottner, F., "Steady Performance Measurements of a Turbofan Engine with Inlet Distortions Containing Co- and Counterrotating Swirl from an Intake Diffuser for Hypersonic Flight," *Journal of Turbomachinery*, Vol. 123, No. 2, 2001, pp. 379–385.

[6] Miller, M. F., Kessler, W. J., and Allen, M. G., "Diode Laser-Based Air Mass Flux Sensor for Subsonic Aeropropulsion Inlets," *Applied Optics*, Vol. 35, No. 24, 1996, pp. 4905–4912.

[7] Allen, M. G., Miller, M. F., and Upschulte, B. L., "Diode Laser Sensors for Aeroengines: Lessons Learned and Future Promises," AIAA Paper 98-2775, June 1998.

[8] White, F. M., *Viscous Fluid Flow*, 2nd ed., McGraw–Hill, Boston, 1991, pp. 429–430.

[9] Abernethy, R. B., Roberts, J., Adams, G., and Steurer, J., "Uncertainty of In-Flight Thrust Determination," SAE AIR 1678, Report of SAE Committee E-33, Society of Automotive Engineers, 1985.

N. Clemens
Associate Editor